

Cuboidal Supraparticles Self-Assembled from Cubic CsPbBr_3 Perovskite Nanocrystals

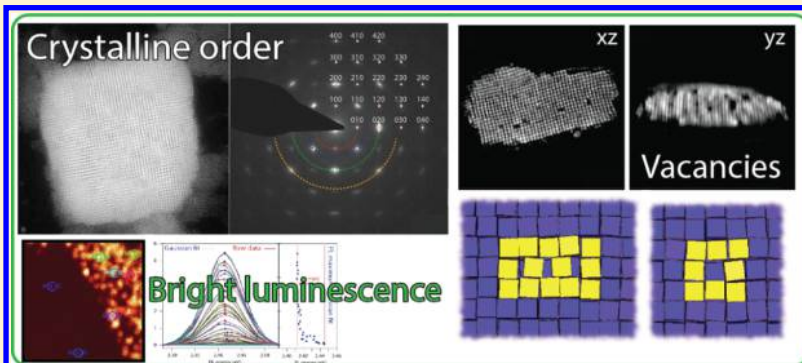
Julia S. van der Burgt,^{†,‡} Jaco J. Geuchies,^{†,‡} Berend van der Meer,[‡] Hans Vanrompay,[§] Daniele Zanaga,[§] Yang Zhang,[§] Wiebke Albrecht,[‡] Andrei V. Petukhov,^{||,‡} Laura Filion,[‡] Sara Bals,[‡] Ingmar Swart,[†] and Daniël Vanmaekelbergh^{*,†}

[†]Condensed Matter and Interfaces, Debye Institute for Nanomaterials Science, [‡]Soft Condensed Matter, Debye Institute for Nanomaterials Science, and ^{||}Physical and Colloidal Chemistry, Debye Institute for Nanomaterials Science, Utrecht University, Utrecht 3508 TA, Netherlands

[§]Electron Microscopy for Materials Science, University of Antwerp, Antwerp 2000, Belgium

^{*}Laboratory of Physical Chemistry, Department of Chemical Engineering and Chemistry, Eindhoven University of Technology, Eindhoven 5612 AZ, Netherlands

Supporting Information



ABSTRACT: Colloidal CsPbBr_3 nanocrystals (NCs) have emerged as promising candidates for various opto-electronic applications, such as light-emitting diodes, photodetectors, and solar cells. Here, we report on the self-assembly of cubic NCs from an organic suspension into ordered cuboidal supraparticles (SPs) and their structural and optical properties. Upon increasing the NC concentration or by addition of a nonsolvent, the formation of the SPs occurs homogeneously in the suspension, as monitored by *in situ* X-ray scattering measurements. The three-dimensional structure of the SPs was resolved through high-angle annular dark-field scanning transmission electron microscopy and electron tomography. The NCs are atomically aligned but not connected. We characterize NC vacancies on superlattice positions both in the bulk and on the surface of the SPs. The occurrence of localized atomic-type NC vacancies—instead of delocalized ones—indicates that NC–NC attractions are important in the assembly, as we verify with Monte Carlo simulations. Even when assembled in SPs, the NCs show bright emission, with a red shift of about 30 meV compared to NCs in suspension.

Over the past decade, a lot of research has been devoted to the properties and improvement of hybrid organic–inorganic perovskite materials (e.g., $\text{CH}_3\text{NH}_3\text{PbX}_3$, X = Cl, Br, or I) for solar cell applications,¹ which has led to an increase in efficiency from 3.8%² to over 20%.³ This success has motivated researchers all over the world to study other types of perovskite materials and extend their optoelectronic applications to photodetectors,^{4,5} light-emitting diodes,^{6–8} and one-⁹ and two-photon¹⁰ pumped gain media for lasers. Recently, cesium lead halide (CsPbX_3) perovskite nanocrystals (NCs) have been reported as a new and promising branch of perovskites. These colloidal NCs can be synthesized with a facile hot injection method and possess bright emission and readily tunable optoelectronic properties.¹¹ In comparison to the hybrid $\text{CH}_3\text{NH}_3\text{PbX}_3$ compounds, the all-inorganic CsPbX_3 has a

better temperature stability.⁵ Moreover these NCs show narrow emission peaks with a full width at half-maximum (fwhm) of 50–80 meV and exhibit quantum yields of up to 90% without any extra passivation of the NC surface.¹² The emission can be tuned over the full visible spectrum by varying the composition of the X-anionic sublattice, either directly or by postsynthetic anion-exchange reactions.^{13–15}

NCs with low polydispersity and high photoluminescence (PL) quantum yields are ideal building blocks for larger structures with predesigned opto-electronic functionalities. In

Received: March 20, 2018

Revised: June 13, 2018

Published: June 14, 2018



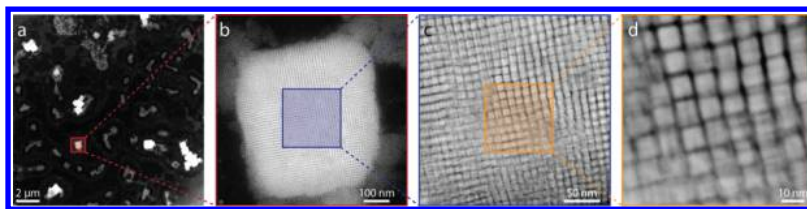


Figure 1. Structure of CsPbBr_3 NC SPs. (a) Low-magnification overview image, showing a relatively low coverage of large, cuboid-shaped SPs. (b) Zoom-in on the marked region in (a) showing a single SP with a nearly cubic shape. (c) Zoom-in on the marked area in (b) showing nearly aligned NCs in a dense cubic stacking. The individual NCs in the SP are clearly visible. (d) Further zoom-in on the marked area in (c). Clearly visible columns of NCs in the lattice of the SP, hinting toward a simple-cubic packing of the constituent NCs inside the SP.

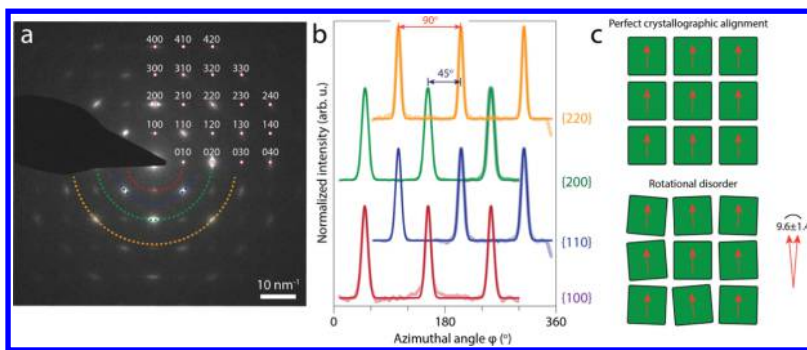


Figure 2. ED analysis of a single SP consisting of CsPbBr_3 NCs. (a) ED pattern acquired along the $[001]$ NC zone axis of the SP shown in Figure 1. The appearance of well-defined diffraction spots indicate that the NCs are atomically aligned. The diffraction spots can be indexed clearly up to reflections from the $\{420\}$ atomic planes. (b) Azimuthal traces at constant scattering vectors q for different atomic reflections, as indicated by the colored semicircles in (a). Fitting the 12 peaks with Gaussian functions (solid lines) gives an average fwhm of $9.6^\circ \pm 1.4^\circ$, which provides an upper limit of the in-plane rotational freedom of the NCs inside the SP. (c) Two-dimensional schemes of a planar section perpendicular to the $[001]$ superlattice axis, demonstrating the effect of slight rotational disorder. The orange arrows represent the $[100]$ atomic axis of each of the nanocubes.

these superlattices, new properties can arise from the electronic and/or magnetic coupling between constituent NCs. For example, the new functionality that arises from the ordered structures of NCs has been used already in magnetic devices¹⁶ and for electronic applications.¹⁷ Here, we report on the self-assembly of cubic-shaped CsPbBr_3 NCs into cuboidal supraparticles (SPs), each SP consisting of several hundreds to thousands of NCs. Using *in situ* X-ray scattering measurements, we show that the SPs nucleate and grow in the solution upon increasing NC concentration or by addition of a nonsolvent. The structure of the superlattices has been studied with (scanning) transmission electron microscopy [(S)TEM], electron diffraction (ED), and high-angle annular dark-field (HAADF) STEM tomography. We show that the NCs form a simple cubic lattice and are atomically aligned but not connected. We observed empty superlattice positions, that is, vacancies similar to those in an atomic crystal, in the bulk as well as on surface lattice positions. Vacancies positioned at the lattice sites should be distinguished from delocalized vacancies predicted for the hard-cube model.¹⁸ Our results thus indicate that attractive interactions between the constituent NCs are important in the self-assembly process. We studied the PL of individual SPs with confocal microspectroscopy. Despite the fact that exciton energy transfer can occur, the SPs still show a bright PL, red-shifted by 30 meV compared to a diluted NC solution.

RESULTS AND DISCUSSION

Formation of Cuboidal SPs. In general, two methods can be used to induce aggregation of NCs in solution: (1) solvent evaporation, also shown by Kovalenko and Bodnarchuk,¹⁹ which increases the NC concentration, and (2) addition of

antisolvent, increasing the potential energy per NC. We used methyl acetate as an antisolvent because it is one of the few polar solvents that does not damage the NCs.²⁰ The use of other polar media, such as methanol, ethanol, acetone, and acetonitrile, as an antisolvent leads to dissolution of the individual NCs. Both methods give identical SPs, however larger SP sizes are obtained by solvent evaporation (see the Supporting Information, Figure S4). The drawback of solvent evaporation is that the SP formation takes rather long (>1 month at room temperature). When we consider self-assembly in a reasonable lab-time period of hours, care has to be taken to operate the assembly under nearly reversible conditions, as fast kinetics can lead to disordered, nonequilibrium structures. Indeed, we observed large clusters with an irregular shape and disordered structure on the NC length scale, when a relatively high amount of antisolvent was added (see the Supporting Information, Figure S5) to speed up the SP formation. The structures that we will discuss were obtained under nearly reversible conditions. A more detailed description of the parameters, which were used during the self-assembly process, can be found in the Supporting Information.

Figure 1 shows self-assembled NC SPs in a series of HAADF-STEM images with increasing magnification. A low magnification image is presented in Figure 1a. The SPs appear as large white cuboids on a dark background. At higher magnifications, it becomes clear that each SP consists of several hundreds of NCs (Figure 1b–d). Moreover, the columns of NCs are clearly distinguished at the highest magnification image (Figure 1d). The degree of ordering inside the SP is apparent through the observed contrast in the HAADF-STEM images, hinting toward a simple cubic stacking of the NCs inside the cuboidal SP. The NCs are clearly not atomically

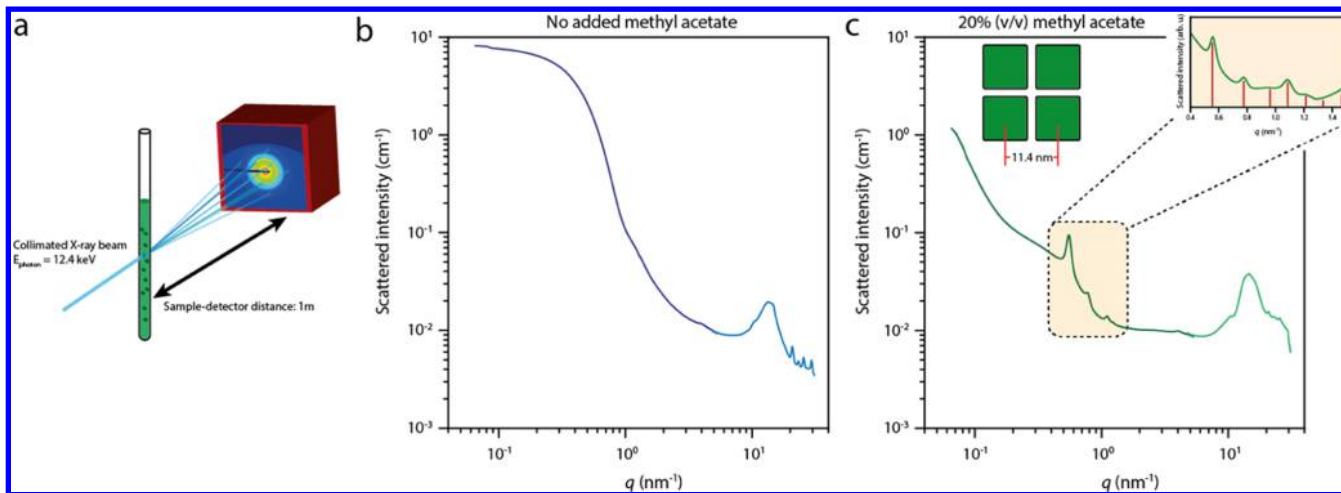


Figure 3. Transmission X-ray scattering of NC solutions during the formation of SPs. (a) Scheme of the experimental setup. A quartz capillary is loaded with a solution of NCs and placed in a LINKAM stage, which is located 1 m from the detector to collect the SAXS signal. The formation of SPs can be initiated by addition of an antisolvent. (b) SAXS pattern of the NC dispersion without addition of the antisolvent, showing only form factor scattering of the individual NCs in solution. (c) SAXS pattern of the diluted NC solution after 3 days of incubation upon addition of 20% (v/v) of methyl acetate antisolvent; the Bragg reflections indicate the formation of crystalline SPs in the solution. The inset shows a zoom on the region with the Bragg peaks, which is scaled by the form factor scattering from (b). The red lines indicate the expected peak positions for a simple-cubic packing of the NCs inside the SPs.

attached as has been observed for superlattices of PbSe NCs,²¹ but they are still separated from each other most likely by their oleate and oleylamine ligands. The alignment must hence be related to the dense cubic stacking of the NC building blocks. The contrast in between the particles seems to be blurred out slightly, which we tentatively ascribe to some positional and rotational disorder of the NCs inside the SP. More images of the formed SPs can be found in the Supporting Information, Figure S3. Although cubic particles can theoretically achieve high packing fractions up to 100%, they are not often encountered in nature. In the CsPbBr₃ SPs discussed here, cubic symmetry emerges over three length scales: on the scale of the atomic lattice, the NC building blocks in the supra particle superlattice, and the cuboidal shape of the SP itself.

To properly quantify the rotational freedom of the CsPbBr₃ NCs inside the SPs, we performed ED experiments on the SP presented in Figure 1. The selected area ED pattern is shown in Figure 2a. The presence of well-defined diffraction spots, instead of powder rings, already indicates that the particles are (nearly) atomically aligned, with the three [001] type zone-axes directed in the principal directions of the NC superlattice (i.e., one of the NC {100} facets pointing upward). The diffraction pattern can be indexed up to reflections from the {420} atomic planes. In Figure 2b, azimuthal traces at the constant scattering vector \mathbf{q} are presented for reflections from the {100}, {110}, {200}, and {220} planes (depicted in red, blue, green, and yellow, respectively). The 12 peaks are fitted with Gaussian functions to obtain an average fwhm of $9.6^\circ \pm 1.4^\circ$, which reflects an upper limit of their in-plane rotational freedom. The high degree of atomic alignment of the NCs inside the SPs originates from the densest possible stacking of NC building blocks with a uniform cubic shape and size.

It is also relevant to characterize the structure of the NC assemblies formed in the suspension before they are scooped and dried on a transmission electron microscopy grid. Therefore, we performed *in situ* transmission small/wide-angle X-ray scattering (SAXS, WAXS) measurements on pure stable NC suspensions and on suspensions in which the NC

assembly was initiated by adding methyl acetate as an antisolvent. A schematic of the experiment is shown in Figure 3a. A solution of NCs is added into a quartz capillary with an outer diameter of 1.5 mm and placed inside a LINKAM stage, positioned at a distance of 1 m from the SAXS detector. The WAXS detector, collecting the atomic diffraction of the NCs, was positioned at the inlet of the vacuum tube holding the SAXS detector. The SAXS and WAXS patterns of a stable suspension are shown in Figure 3b. The SAXS region (light blue) only shows form factor scattering from dispersed NCs. The WAXS signal (dark blue) shows sharp diffraction peaks originating from the atomic perovskite lattice of the NCs. A sample with a volume fraction of 0.2 methyl acetate was measured after 3 days of incubation and is presented in Figure 3c. The SAXS pattern shows clear Bragg peaks at positions of 0.55, 0.78, 1.1, and 1.23 nm⁻¹. Their relative peak positions correspond to $1:\sqrt{2}:2:\sqrt{5}$, which corresponds to scattering from the {100}, {110}, {200}, and {210} lattice planes of a simple cubic lattice of NCs. The measured NC–NC distance inside the SPs in suspension is determined to be 11.4 ± 0.1 nm, corresponding to NCs still separated by their oleate and oleylamine ligands. The fwhm of the {100} reflection is 0.378 nm⁻¹, which corresponds to spatial extension of the periodic order of roughly 166.3 nm. The SP formation is reversible, as the constituent NCs readily redisperse upon diluting the solution of SPs (see the Supporting Information, Figure S6).

Recent work by Bertolotti et al. also showed that the CsPbBr₃ NCs have the tendency to stack in solution,²² similar to concentrated solutions of perovskite nanoplates.²³ They argue that the stacking direction occurs most likely in the {100} NC direction, similar to the NCs in the SPs in this work. Others have also found that these perovskite NCs readily assemble into one-dimensional chains by addition of molecular clusters^{24,25} or through ligand–solvent interactions.²⁶ Such stacks could hence be a precursor phase in the formation of the SPs presented in this work. However, this remains to be verified by performing *in situ* time-resolved SAXS and WAXS

on the self-assembly process, which is beyond the scope of this article.

NC Vacancies inside a SP Studied with HAADF-STEM Tomography and Monte Carlo Simulations. To study the geometric structure of the NCs inside the SPs in more detail, a single SP was studied using HAADF-STEM tomography. A series of projection images was acquired with an angular range of -70° to 78° and a tilt increment of 2° . Orthogonal to that, a second tilt series was acquired from -76° to 76° to reduce the missing wedge of tilt angles to a missing pyramid.²⁷ Using this dual tilt series as an input for several mathematical reconstruction algorithms, we found that the quality of the reconstruction was greatly improved compared to the reconstruction that was obtained from just using the one tilt series.

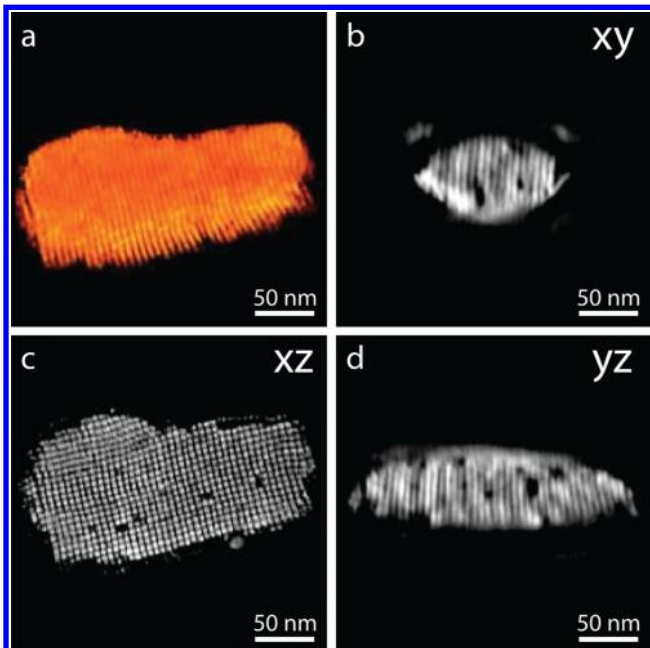


Figure 4. Looking inside SPs with HAADF-STEM tomography. (a) Visualization of the three-dimensional reconstruction of a single SP, acquired by rotating the sample over two orthogonal tilt series and reconstructed using a SIRT algorithm. Orthoslices through the xy (b), xz (c), and yz (d) directions of the tomogram reveal several localized NC vacancies and groups of missing NCs in the bulk of the SP. All vacancies are clearly defined on a lattice position.

A visualization of the acquired tomogram is presented in Figure 4a. Unfortunately, we are not able to clearly resolve all individual NC positions inside the SP; the missing pyramid of tilt angles smears out the information in the z -direction of the cuboidal SP. Nonetheless, the orthoslices taken through the center of the structure in Figure 4b–d show interesting features. In all three orthogonal directions, we observe empty places on lattice positions. They appear to be localized single point vacancies and vacancy clusters. From the tomogram, we are able to estimate the volume fraction of vacancies in the bulk of the SP of 3.3%, assuming cubic symmetry of the NC lattice (see the Supporting Information for more details). Furthermore, we also performed secondary electron-STEM to acquire information on the surface of the SPs, which can be found in the Supporting Information (Figures S7 and S8). Also, on the surface of the SPs, we observe localized NC

vacancies and groups of missing NCs. We estimate that the amount of missing surface NCs roughly equals $5.5 \pm 1.5\%$.

Interestingly, the localized nature of the NC vacancies is in contrast to previous Monte Carlo and molecular dynamics simulations for hard cubes, that is, cubes that interact only through excluded volume interactions. Smalleenburg et al. showed that for hard cubes, vacancies manifest themselves as a finite-length chain of particles along one of the principal axes in the crystal.¹⁸ The vacancy is thus spread over many lattice positions. More specifically, in this hard-cube system, the equilibrium concentration of vacancies is very high (up to 6%) because of the fact that creating a vacancy provides additional free volume for multiple nearby particles, which increases the entropy of the crystal. Note that in a system of attractive cubes, Rossi et al. observed localized NC vacancies, where colloidal cubes of roughly 1 micron are self-assembled into simple cubic lattices through addition of a depletant, which induces effective attractions between the cube facets.²⁸ As such, we propose that the localization and grouping of NC vacancies in our experiments point toward attractive interactions between the NCs during the self-assembly. Specifically, for sufficiently large NC–NC attractions, the free energy will be minimized when the particles in the vicinity of the vacancy are sitting on regular lattice positions, as the cost of breaking cohesive bonds will dominate over the entropic gain associated with vacancy delocalization.

To understand the observed localization of the vacancies, we performed Monte Carlo simulations of cubes in the NVT ensemble, where N (the number of particles), V (the volume), and T (the temperature) are fixed, and the cube–cube attraction can be changed from zero to several times the thermal energy. As a minimal model that captures the repulsive core and attraction, we model the interactions between the

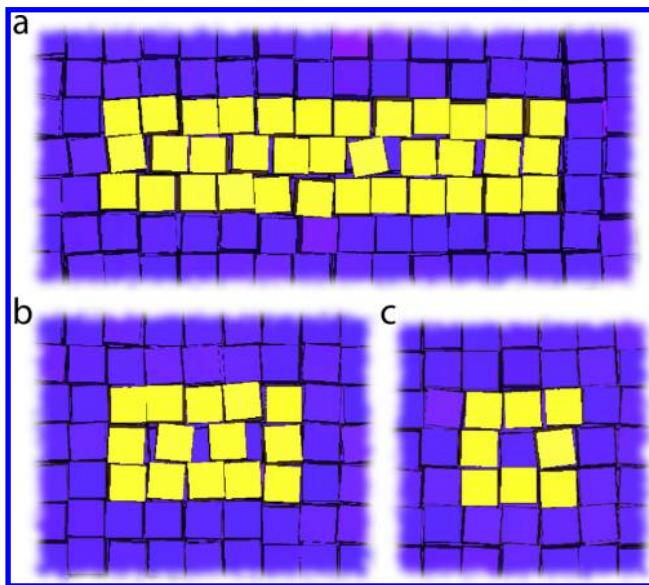


Figure 5. Monte Carlo simulations of (de)localized NC vacancies inside the SPs as a function of the attraction strength. (a) $\epsilon = 0 k_b T$, the NC vacancy is delocalized over many lattice positions. (b) $\epsilon = -0.5 k_b T$, long delocalized NC vacancies are not observed anymore, only weak delocalization of the NC vacancies over a maximum of a few lattice sites are observed. (c) $\epsilon = -1 k_b T$, NC vacancies are exclusively observed on lattice positions and do not delocalize. The latter is also observed in the tomography experiments presented in Figure 4.

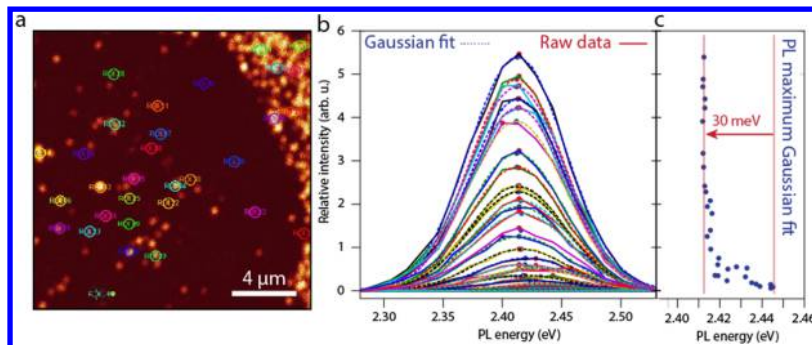


Figure 6. Confocal microspectroscopy on individual CsPbBr_3 NC SPs. (a) Confocal micrograph of a glass slide covered with SPs, which appear as high intensity areas on a dark background. The circles indicate the areas in which the PL signal was integrated. (b) PL spectra of a large number of different regions in the confocal micrograph shown in (a). The solid lines indicate raw data, whereas the dashed lines are Gaussian fits to the data. (c) Comparing the peak intensity to the PL energy, a red shift of roughly 30 meV is observed for the SPs compared to the NC monolayer background.

cubes as a combination of a cubic hard-core repulsion and a spherically-symmetric square well attraction originating from the center of the cube. The range of the attractive square well was fixed to $\Delta = 1.14\sigma$, with σ is the edge length of the cubes, and we varied the well depth $\beta\epsilon$, with $\beta = 1/k_b T$. Thus, for $\beta\epsilon = 0$, our model reduces to the hard-cube model with delocalized vacancies, and we can study the effect of increasing the attraction strength $\beta\epsilon$ on the vacancy structure. While the nucleation of these SPs is described in the *Supporting Information* (Figure S12), we will now focus on the (de)localization of defects in the bulk of the crystal. In these simulations, we start off from a perfect simple cubic crystal at a fixed packing fraction of $\varphi = 0.80$ and initialized a single vacancy by removing a single particle. In agreement with ref 22 we observe NC vacancies to be delocalized over many lattice positions for the hard-cube system, $\beta\epsilon = 0$ (Figure 5a). Yet, upon introducing a slight attraction between the cubes, $\beta\epsilon = -0.5$, the long delocalized NC vacancies are not observed anymore (Figure 5b). Instead, the NC vacancies spread only over a couple of lattice sites. Thus, already for a moderate attraction strength between the particles, we observe the defect structure to be dominated by the cohesive bonds between the particles. For slightly larger attractions, $\beta\epsilon = -1$, we observe the particles in the vicinity of the NC vacancies exclusively on lattice positions, and no delocalized NC vacancies are observed (Figure 5c), similar to the tomography experiments presented in Figure 4.

Optical Properties of SPs Compared to NCs in Solution. Often, quantum dot (QD) solids suffer from a reduced PL quantum yield, as exciton energy transfer between the NCs in the solid enhances the probability of nonradiative energy transfer. We found that CsPbBr_3 SPs deposited on a glass slide remained strongly emissive, with a PL quantum yield of 26%, as determined with an integrating sphere. This is good news for several opto-electronic applications requiring a QD solid as the optically active material. To study the optical properties of individual SPs in more detail, we performed confocal microspectroscopy. A dispersion containing the SPs was drop-cast on a microscope slide, and the solvent of the dispersion was allowed to evaporate. A droplet of immersion oil was placed on the sample, and a second cover slide was placed on top of the sample. The results are presented in Figure 6 and in the *Supporting Information*, Figure S13.

Figure 6 shows the PL spectra of many spots observed on the glass slide. Figure 6a shows the confocal micrograph of a

glass slide covered with SPs. The circled areas indicate the regions where the PL signal was integrated. In Figure 6b, we present the peak energies of 30 spots versus the intensity and observe a gradual red shift (shown in Figure 6c), which abruptly becomes constant at a sufficiently high spot intensity, the overall red shift being roughly 30 meV. A similar red shift is observed when the PL spectra of dispersed NCs and dispersed SPs are compared (*Supporting Information*, Figures S14 and S15). We hence conclude that the bright spots present regions of SPs and the weak spots present individual NCs or smaller clusters.

The red shift observed in the emission of the SPs with respect to individual NCs could have several causes: Kovalenko and Bodnarchuk reported in their recent work¹⁹ that the relative increase in the dielectric constant of the NC environment can cause a red shift if the electron and hole both become more delocalized. Furthermore, the excitons in the NCs are in the weak confinement regime; the electronic coupling between NCs inside a SP could thus also cause a weak red shift of the PL spectrum. Third, exciton energy transfer results in a spatial diffusion of the excitons over the superlattice, always with a trend toward lower exciton energy. Di Stasio et al. reported a similar shift of the PL in concentrated solutions of CsPbBr_3 NCs and solid-state films.²⁹ This effect is also shown in concentrated solutions of the cubic CsPbBr_3 NCs and is reversible upon diluting the NC dispersion.³⁰ In our time-resolved PL experiments (Figure S14), we observe that the shift in the PL peak position occurs faster than the time resolution of our setup (~ 250 ps), which is probably faster than the exciton energy transfer. This indicates that energy transfer is not the cause for the observed red shift. We must conclude here that although the red shift occurring in CsPbBr_3 NC SPs is well-established, its main cause remains an outstanding question.

In summary, we have shown that CsPbBr_3 nanocubes self-assemble into SPs that have an overall cuboidal shape. In the superlattices, the NCs are atomically aligned but separated by the capping ligands. Vacancies form real point defects instead of being delocalized, indicating that attractive interactions play a role in the self-assembly process. The SPs show a bright PL, red-shifted by 30 meV with respect to that of individual NCs. The fact that the obtained SPs are still highly emissive makes them promising candidates for opto-electronic applications. For example, they possibly can be used as microcavities to study the confinement of the PL and lasing inside SPs.

■ ASSOCIATED CONTENT

§ Supporting Information

The Supporting Information is available free of charge on the ACS Publications website at DOI: [10.1021/acs.jpcc.8b02699](https://doi.org/10.1021/acs.jpcc.8b02699).

Synthesis of CsPbBr₃ NCs, purification of the NCs, self-assembly of the NC solutions into SPs, transmission SAXS and WAXS experiments, and optical spectroscopy ([PDF](#))

■ AUTHOR INFORMATION

Corresponding Author

*E-mail: d.vanmaekelbergh@uu.nl.

ORCID

Andrei V. Petukhov: [0000-0001-9840-6014](#)

Sara Bals: [0000-0002-4249-8017](#)

Daniël Vanmaekelbergh: [0000-0002-3535-8366](#)

Author Contributions

[#]J.S.v.d.B. and J.J.G. contributed equally.

Notes

The authors declare no competing financial interest.

■ ACKNOWLEDGMENTS

The authors thank Dr. Rajeev Dattani and Jacques Gorini from the ID02 beamline of the ESRF for their excellent assistance during the X-ray scattering experiments. We also thank Carlo van Overbeek, P. Tim Prins, and Federico Montanarella for their support during the synchrotron experiments. The authors gratefully acknowledge Prof. Dr. Alfons van Blaaderen for fruitful discussions. D.V. acknowledges funding from NWO-CW TOPPUNT “Superficial superstructures.” J.J.G. acknowledges the joint Debye and ESRF graduate programs for the financial support. H.V. gratefully acknowledges the financial support by the Flemish Fund for Scientific Research (FWO grant 1S32617NN). S.B. acknowledges the financial support from the European Research Council (ERC Starting grant #335078-COLOURATOMS). Y.Z. acknowledges the financial support from the European Union’s Horizon 2020 research and innovation program, under the Marie Skłodowska-Curie grant agreement #665501 through a FWO [PEGASUS]2 Marie Skłodowska-Curie fellowship (12U4917N). W.A. acknowledges the financial support from the European Research Council under the European Unions Seventh Framework Program (FP-2007-2013)/ERC Advanced grant agreement 291667 HierarSACol.

■ REFERENCES

- (1) Kulpak, M.; Cahen, D.; Hodes, G. How Important Is the Organic Part of Lead Halide Perovskite Photovoltaic Cells? Efficient CsPbBr₃ Cells. *J. Phys. Chem. Lett.* **2015**, *6*, 2452–2456.
- (2) Kojima, A.; Teshima, K.; Shirai, Y.; Miyasaka, T. Organometal Halide Perovskites as Visible-Light Sensitizers for Photovoltaic Cells. *J. Am. Chem. Soc.* **2009**, *131*, 6050–6051.
- (3) Eperon, G. E.; Leijtens, T.; Bush, K. A.; Prasanna, R.; Green, T.; Wang, J. T.; McMeekin, D. P.; Volonakis, G.; Milot, R. L.; May, R.; et al. Perovskite-Perovskite Tandem Photovoltaics with Optimized Bandgaps. *Science* **2016**, *354*, 861.
- (4) Gao, J.; Nguyen, S. C.; Bronstein, N. D.; Alivisatos, A. P. Solution-Processed, High-Speed, and High-Quantum-Efficiency Quantum Dot Infrared Photodetectors. *ACS Photonics* **2016**, *3*, 1217–1222.

(5) Ramasamy, P.; Lim, D.-H.; Kim, B.; Lee, S.-H.; Lee, M.-S.; Lee, J.-S. All-Inorganic Cesium Lead Halide Perovskite Nanocrystals for Photodetector Applications. *Chem. Commun.* **2016**, *52*, 2067–2070.

(6) Wang, N.; Cheng, L.; Ge, R.; Zhang, S.; Miao, Y.; Zou, W.; Yi, C.; Sun, Y.; Cao, Y.; Yang, R.; et al. Perovskite light-emitting diodes based on solution-processed self-organized multiple quantum wells. *Nat. Photonics* **2016**, *10*, 699–704.

(7) Wang, P.; Bai, X.; Sun, C.; Zhang, X.; Zhang, T.; Zhang, Y. Multicolor Fluorescent Light-Emitting Diodes Based on Cesium Lead Halide Perovskite Quantum Dots. *Appl. Phys. Lett.* **2016**, *109*, 063106.

(8) Zhang, X.; Lin, H.; Huang, H.; Reckmeier, C.; Zhang, Y.; Choy, W. C. H.; Rogach, A. L. Enhancing the Brightness of Cesium Lead Halide Perovskite Nanocrystal Based Green Light-Emitting Devices through the Interface Engineering with Perfluorinated Ionomer. *Nano Lett.* **2016**, *16*, 1415–1420.

(9) Yakunin, S.; Protesescu, L.; Krieg, F.; Bodnarchuk, M. I.; Nedelcu, G.; Humer, M.; De Luca, G.; Fiebig, M.; Heiss, W.; Kovalenko, M. V. Low-Threshold Amplified Spontaneous Emission and Lasing from Colloidal Nanocrystals of Caesium Lead Halide Perovskites. *Nat. Commun.* **2015**, *6*, 8056.

(10) Xu, Y.; Chen, Q.; Zhang, C.; Wang, R.; Wu, H.; Zhang, X.; Xing, G.; Yu, W. W.; Wang, X.; Zhang, Y.; et al. Two-Photon-Pumped Perovskite Semiconductor Nanocrystal Lasers. *J. Am. Chem. Soc.* **2016**, *138*, 3761–3768.

(11) Lignos, I.; Stavrakis, S.; Nedelcu, G.; Protesescu, L.; deMello, A. J.; Kovalenko, M. V. Synthesis of Cesium Lead Halide Perovskite Nanocrystals in a Droplet-Based Microfluidic Platform: Fast Parametric Space Mapping. *Nano Lett.* **2016**, *16*, 1869–1877.

(12) Protesescu, L.; Yakunin, S.; Bodnarchuk, M. I.; Krieg, F.; Caputo, R.; Hendon, C. H.; Yang, R. X.; Walsh, A.; Kovalenko, M. V. Nanocrystals of Cesium Lead Halide Perovskites (CsPbX₃, X = Cl, Br, and I): Novel Optoelectronic Materials Showing Bright Emission with Wide Color Gamut. *Nano Lett.* **2015**, *15*, 3692–3696.

(13) Nedelcu, G.; Protesescu, L.; Yakunin, S.; Bodnarchuk, M. I.; Grotevent, M. J.; Kovalenko, M. V. Fast Anion-Exchange in Highly Luminescent Nanocrystals of Cesium Lead Halide Perovskites (CsPbX₃, X = Cl, Br, I). *Nano Lett.* **2015**, *15*, 5635–5640.

(14) Akkerman, Q. A.; D’Innocenzo, V.; Accornero, S.; Scarpellini, A.; Petrozza, A.; Prato, M.; Manna, L. Tuning the Optical Properties of Cesium Lead Halide Perovskite Nanocrystals by Anion Exchange Reactions. *J. Am. Chem. Soc.* **2015**, *137*, 10276–10281.

(15) Koscher, B. A.; Bronstein, N. D.; Olshansky, J. H.; Bekenstein, Y.; Alivisatos, A. P. Surface- vs Diffusion-Limited Mechanisms of Anion Exchange in CsPbBr₃ Nanocrystal Cubes Revealed through Kinetic Studies. *J. Am. Chem. Soc.* **2016**, *138*, 12065.

(16) Dong, A.; Chen, J.; Vora, P. M.; Kikkawa, J. M.; Murray, C. B. Binary Nanocrystal Superlattice Membranes Self-Assembled at the Liquid-Air Interface. *Nature* **2010**, *466*, 474–477.

(17) Dong, A.; Jiao, Y.; Milliron, D. J. Electronically Coupled Nanocrystal Superlattice Films by in Situ Ligand Exchange at the Liquid-Air Interface. *ACS Nano* **2013**, *7*, 10978–10984.

(18) Smalleenburg, F.; Filion, L.; Marechal, M.; Dijkstra, M. Vacancy-Stabilized Crystalline Order in Hard Cubes. *Proc. Natl. Acad. Sci. U.S.A.* **2012**, *109*, 17886–17890.

(19) Kovalenko, M. V.; Bodnarchuk, M. I. Lead Halide Perovskite Nanocrystals: From Discovery to Self-Assembly and Applications. *Chim. Int. J. Chem.* **2017**, *71*, 461–470.

(20) Swarnkar, A.; Marshall, A. R.; Sanehira, E. M.; Chernomordik, B. D.; Moore, D. T.; Christians, J. A.; Chakrabarti, T.; Luther, J. M. Quantum Dot-Induced Phase Stabilization of α -CsPbI₃ Perovskite for High-Efficiency Photovoltaics. *Science* **2016**, *354*, 92.

(21) Evers, W. H.; Goris, B.; Bals, S.; Casavola, M.; de Graaf, J.; van Roij, R.; Dijkstra, M.; Vanmaekelbergh, D.; Vanmaekelbergh, D. Low-Dimensional Semiconductor Superlattices Formed by Geometric Control over Nanocrystal Attachment. *Nano Lett.* **2013**, *13*, 2317–2323.

(22) Bertolotti, F.; Protesescu, L.; Kovalenko, M. V.; Yakunin, S.; Cervellino, A.; Billinge, S. J. L.; Terban, M. W.; Pedersen, J. S.; Masciocchi, N.; Guagliardi, A. Coherent Nanotwins and Dynamic

Disorder in Cesium Lead Halide Perovskite Nanocrystals. *ACS Nano* **2017**, *11*, 3819.

(23) Bekenstein, Y.; Koscher, B. A.; Eaton, S. W.; Yang, P.; Alivisatos, A. P. Highly Luminescent Colloidal Nanoplates of Perovskite Cesium Lead Halide and Their Oriented Assemblies. *J. Am. Chem. Soc.* **2015**, *137*, 16008–16011.

(24) Zhang, X.; Lv, L.; Ji, L.; Guo, G.; Liu, L.; Han, D.; Wang, B.; Tu, Y.; Hu, J.; Yang, D.; et al. Self-Assembly of One-Dimensional Nanocrystal Superlattice Chains Mediated by Molecular Clusters. *2016*.138.3290. DOI: [10.1021/jacs.6b00055](https://doi.org/10.1021/jacs.6b00055)

(25) Zhang, X.; Lv, L.; Wu, G.; Yang, D.; Dong, A. Cluster-Mediated Assembly Enables Step-Growth Copolymerization from Binary Nanoparticle Mixtures with Rationally Designed Architectures. *Chem. Sci.* **2018**, *9*, 3986–3991.

(26) Soetan, N.; Erwin, W. R.; Tonigan, A. M.; Walker, D. G.; Bardhan, R. Solvent-Assisted Self-Assembly of CsPbBr₃ Perovskite Nanocrystals into One-Dimensional Superlattice. *J. Phys. Chem. C* **2017**, *121*, 18186–18194.

(27) Arslan, I.; Tong, J. R.; Midgley, P. A. Reducing the Missing Wedge: High-Resolution Dual Axis Tomography of Inorganic Materials. *Ultramicroscopy* **2006**, *106*, 994–1000.

(28) Rossi, L.; Sacanna, S.; Irvine, W. T. M.; Chaikin, P. M.; Pine, D. J.; Philipse, A. P. Cubic Crystals from Cubic Colloids. *Soft Matter* **2011**, *7*, 4139–4142.

(29) Di Stasio, F.; Imran, M.; Akkerman, Q. A.; Prato, M.; Manna, L.; Krahne, R. Reversible Concentration-Dependent Photoluminescence Quenching and Change of Emission Color in CsPbBr₃ Nanowires and Nanoplatelets. *J. Phys. Chem. Lett.* **2017**, *8*, 2725–2729.

(30) de Weerd, C.; Gomez, L.; Zhang, H.; Buma, W. J.; Nedelcu, G.; Kovalenko, M. V.; Gregorkiewicz, T. Energy Transfer between Inorganic Perovskite Nanocrystals. *J. Phys. Chem. C* **2016**, *120*, 13310–13315.

Supporting Information

Cuboidal supraparticles self-assembled from cubic CsPbBr_3 perovskite nanocrystals

Julia S. van der Burgt^{1}, Jaco J. Geuchies^{1*}, Berend van der Meer², Hans Vanrompay³,
Daniele Zanaga³, Yang Zhang³, Wiebke Albrecht², Andrei V. Petukhov^{4,5}, Laura Filion², Sara
Bals³, Ingmar Swart¹, Daniël Vanmaekelbergh¹*

1. Condensed Matter and Interfaces, Debye Institute for Nanomaterials Science, Utrecht University
2. Soft Condensed Matter, Debye Institute for Nanomaterials Science, Utrecht University
3. Electron Microscopy for Materials Science, University of Antwerp
4. Physical and Colloidal Chemistry, Debye Institute for Nanomaterials Science, Utrecht University
5. Laboratory of Physical Chemistry, Department of Chemical Engineering and Chemistry, Eindhoven University of Technology

*These authors contributed equally

METHODS

Synthesis of CsPbBr₃ nanocrystals (NCs). The CsPbBr₃ NCs were prepared according to the method described by Protesescu *et al.*¹ First, Cs-oleate precursor stock solution was prepared. Cs₂CO₃ (0.814g, 99%, Aldrich), 2.5 mL OA (90%, Aldrich) and 40 mL ODE (90%, Aldrich) were loaded into a 100 mL round-bottom flask. The mixture was dried under vacuum for approximately 1h at 120 °C, and then heated under N₂ to 150 °C until all Cs₂CO₃ had reacted with OA. ODE (5 mL) and PbBr₂ (0.069g, 99.999%, Aldrich) were loaded into a separate 25 mL flask and dried under vacuum for 1h at 120 °C. OLAM (0.5 mL, 70%, Aldrich) and OA (0.5 mL) were injected at 120 °C under N₂ atmosphere. After PbBr₂ had dissolved, the temperature was raised to 180 °C and a 0.4 mL portion of the Cs-oleate stock solution was quickly injected. We note that the Cs-oleate stock solution had to be preheated to ~100 °C before injection. After five to ten seconds the reaction mixture was cooled by an ice-water bath in order to quench the reaction. The size of the nanocubes was determined as described in Figure S1.

Purification of the nanocrystals. The CsPbBr₃ NCs were purified following the method described by De Roo *et al.*⁶¹ (for a synthesis based on 69 mg of PbBr₂). The crude synthesis solution was centrifuged for 3 min at 10 000 rpm and the colored supernatant was discarded. Then, 300 µL of hexane was added and the NCs were dispersed using a vortex mixer. Subsequently, the suspension was again centrifuged for 3 min at 10 000 rpm, after which the precipitate, containing larger NCs and agglomerates, was discarded. Another 300 µL of hexane was added to the supernatant, resulting in a colloidal dispersion of CsPbBr₃ NCs.

Self-assembly of the NC solutions into supraparticles. The CsPbBr₃ NCs were self-assembled into cuboidal supraparticles by adding a varying amount of methyl acetate into a solution containing 0.1 µM NCs (as determined with absorption spectroscopy¹). The samples were incubated at room temperature in a dark storage area for five days, unless mentioned otherwise. Self-assembly through solvent-evaporation occurred in NC solutions with a concentration higher than 1 µM NCs. Note that

the latter number is a rough estimate, since the exact determination of the concentration was hampered due to saturation of the absorption signal.

Transmission SAXS and WAXS experiments. Small and wide-angle X-ray scattering (SAXS and WAXS) experiments were performed at the ID02 beamline of the European Synchrotron Radiation Facility (ESRF), Grenoble, France. The SAXS detector was a Rayonix MC-170HS mounted at a distance of 1m from the sample inside a vacuum tube to background scattering from air. The WAXS detector was a Rayonic LX-170HS (calibrated with α -Al₂O₃), which was mounted at the beginning of the vacuum tube. The combination of detectors allowed us to measure a q-range of 6.5×10^{-2} nm⁻¹ to 4.8 nm⁻¹. The wavelength of the collimated X-ray beam was 0.1 nm (12.4 keV). A quartz capillary (with an inner diameter of 1 mm and 10 μ m wall thickness) with a NC solution in toluene (or a diluted solution of NCs in toluene with methyl acetate) was placed inside a Linkam stage.

Optical spectroscopy. Samples for optical measurements and time-resolved optical spectroscopy (TRES) were prepared by diluting the colloidal dispersion of NCs with anhydrous toluene under nitrogen and stored in sealed quartz cuvettes. Absorption spectra were measured on a double beam Perkin-Elmer Lambda 16 UV/Vis spectrometer. Photoluminescence (PL) spectra were recorded on an Edinburgh Instruments FLS920 Spectrofluorimeter equipped with a 450 W Xenon lamp as excitation source and double grating monochromators. PL decay curves were obtained by time-correlated single-photon counting on a Hamamatsu H7422-02 photomultiplier tube with low dark count rate (< 10 cts/s). A pulsed diode laser (EPL-445 Edinburgh Instruments, 375 nm, 55 ps pulse width, 0.2 MHz repetition rate) was used as the excitation source.

Confocal microspectroscopy. Individual supraparticles were studied using a Leica TCS SP8 confocal microscope. We used a 63x/1.4 oil-immersion confocal Leica objective. The sample was excited with a fiber-based white light laser at 470 nm. A droplet of the dispersion containing supraparticles was placed on a microscope slide and the solvent (toluene) was allowed to evaporate. A droplet of immersion oil was placed on top of the sample to index-match the oil objective, followed by another

cover microscope slide (with a thickness of 160-190 μm). Another droplet of immersion oil was placed on top of the cover slide before placing the sample into the microscope.

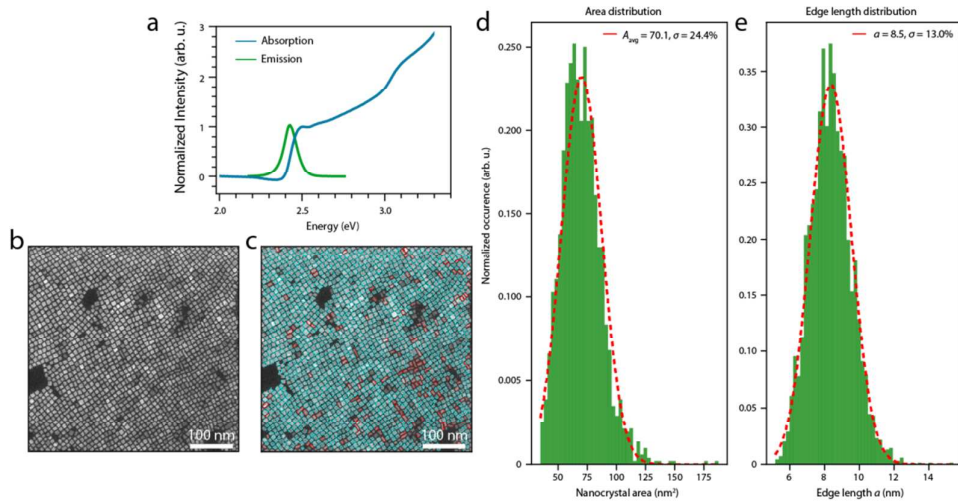


Figure S1: Characterization of the as-synthesized CsPbBr_3 perovskite NCs. (a) Normalized optical absorption (blue) and PL (green) spectra of the as-synthesized nanocubes in toluene. (b) HAADF-STEM image of a sub-monolayer of the NCs. (c) Computer aided image analysis allows us to obtain statistics on the size and shape of the particles. Particles with an aspect ratio ≤ 1.5 are defined as cubic and are outlined with a blue square. Particles with an aspect ratio > 1.5 are defined as platelet-like and are outlined with a red rectangle. (d) Distribution of the areas of the detected NCs. (e) Distribution of the detected edge-lengths of the NCs. Several HAADF-STEM micrographs were used to gather statistics of over 5000 NCs.

We characterized the optical absorption and emission spectra in solution (toluene). Throughout the article we used several different batches of NCs, all showing emission around 2.4 eV with a narrow FWHM (<80 meV). The PL quantum yield varies in between batches in between 85% and 95% as determined with an integrating sphere. Figure S1(a) shows the characteristic absorption and emission spectra for the NCs with an edge length of roughly 8.5 nm. The NCs are in the weak confinement regime (Bohr exciton radius of 3.5 nm) and no clear bulk excitonic peak is visible in the absorption spectrum.

The geometry of the NCs was characterized by high-angle annular dark-field (HAADF) scanning transmission electron microscopy (STEM). We employ a custom made Python code to gather information on the geometry of the synthesized NCs. The process is schematically outlined in Figure S2. After filtering and binarizing the image, the particles are fitted with a rectangle. The results of the particle detection are shown in Figure S1(c). We define particles with an aspect ratio 1.5 as cubic and outline the detected shape with a blue square. Detected particles with an aspect ratio > 1.5 are defined as rectangular, and are

outlined with a red rectangle. Over 95% of the particles in a single HAADF-STEM image are detected, and the resulting outlines seem to match the particle contours very well. Over 5000 particles were analyzed over several HAADF-STEM images, which allowed us to obtain decent statistics on the particle size and shape. The area of the detected particles is shown in Figure S1(d) and the detected nanocube edge-length is shown in Figure S1(e). The acquired data is binned into a histogram and fitted with a normal distribution. The nanocrystals have {100} facets with an average surface area of $70 \pm 17 \text{ nm}^2$ and an edge length of $8.5 \pm 1.1 \text{ nm}$.

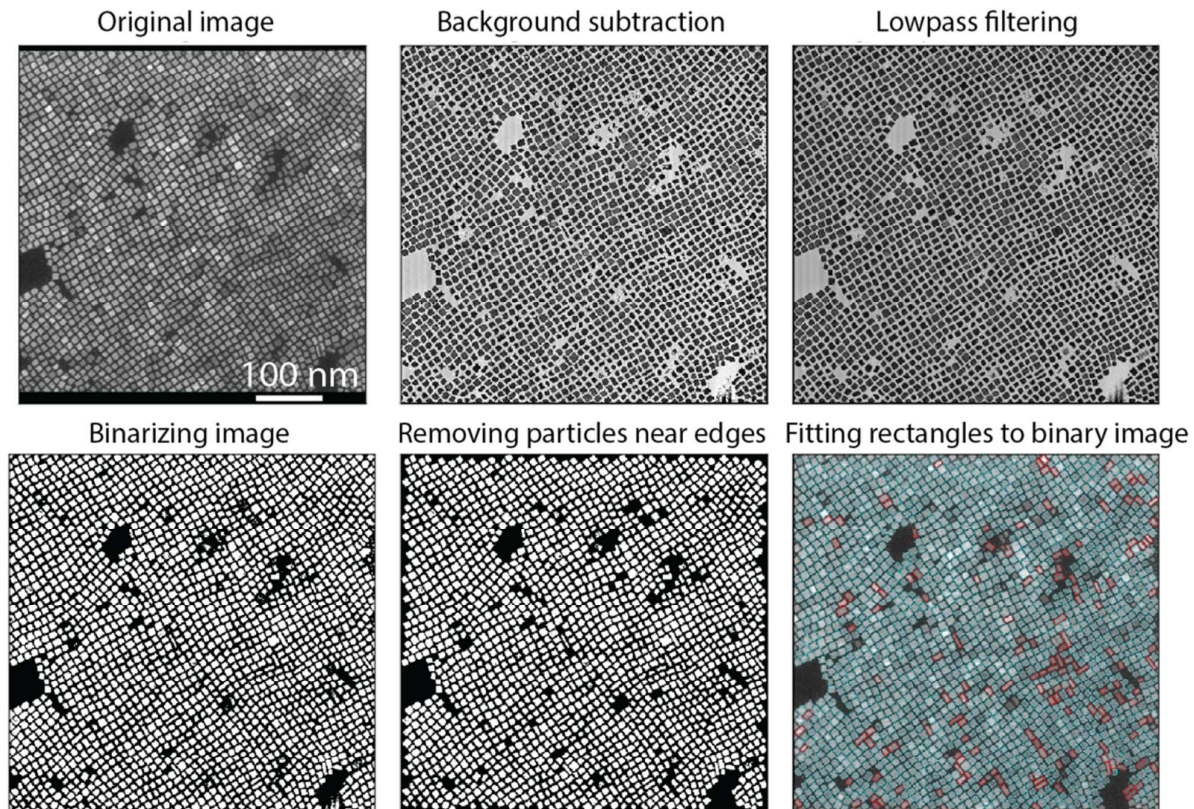


Figure S2: Schematic outline of the used particle detection scheme. An electron micrograph is loaded into the program. The background is detected by fitting each column of the image matrix with a third-order polynomial and this is subtracted from the original. After this the image is low-pass filtered through a Fast-Fourier Transform. The resulting filtered image is binarized and particles near the edges are filtered out, before fitting the binary areas with rectangles. The particles are defined cubic and labeled blue for aspect ratio's ≤ 1.5 . Particles with an aspect ratio > 1.5 are defined as platelet-like and are labeled red.

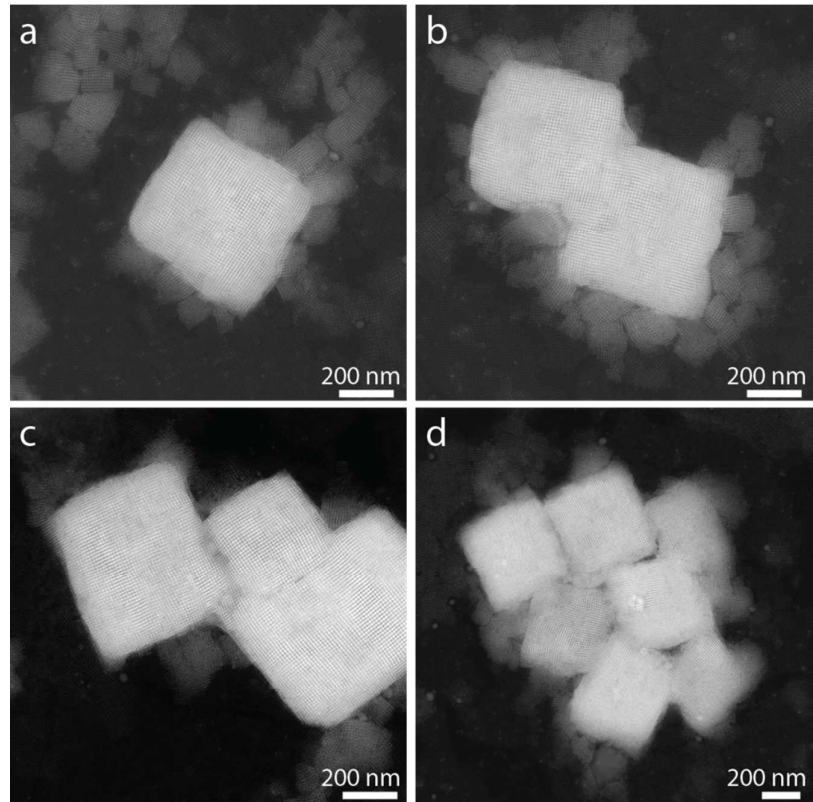


Figure S3: HAADF-STEM overview images of typically encountered supraparticles. (a) Single supraparticles are most commonly observed. **(b)** Micrograph of two aggregated supraparticles. **(c)** Micrograph of three aggregated supraparticles. **(d)** Micrograph of multiple aggregated supraparticles. Note how **(b)** and **(c)** appear the same orientation of the NC lattice, whereas in **(d)** the rotational disorder is larger.

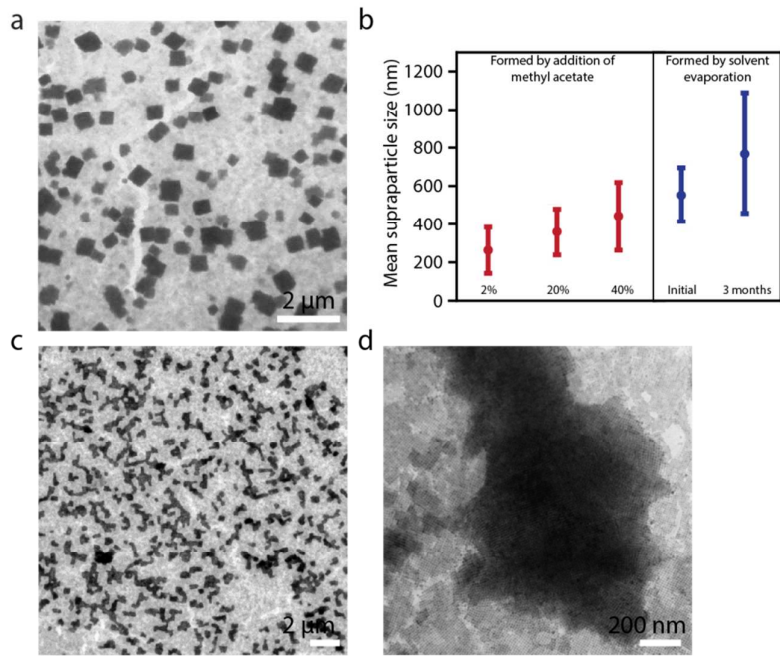


Figure S4: Supraparticle growth over time. **(a)** Bright-field TEM overview image of supraparticles, grown by addition of methyl acetate up to a volume fraction of 0.2. The TEM image was taken one week after addition of methyl acetate. **(b)** Average supraparticle size after one week of growth (for anti-solvent addition), and by solvent evaporation after one month and after three months. The error bars depict the standard deviation of the size dispersion. **(c)** Upon increasing the volume fraction of methyl acetate above 0.4 (here 0.5), the supraparticles possess irregular shapes and **(d)** the NCs appear randomly aggregated.

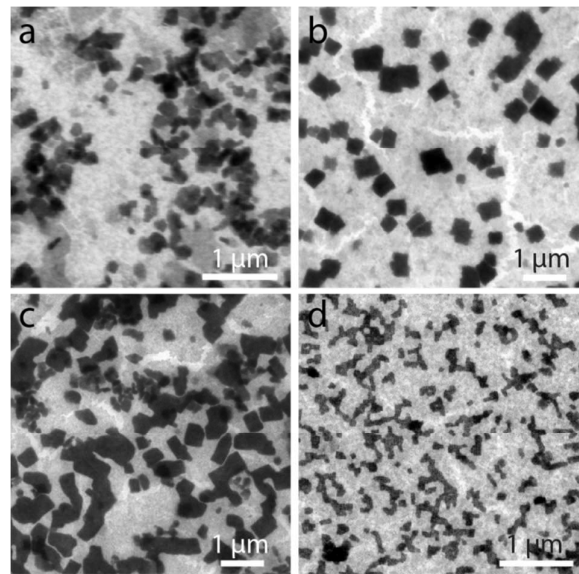


Figure S5: Effect of the amount of added anti-solvent on the supraparticle formation.
From **(a)** to **(d)** we have added a volume fraction of 8%, 20%, 40% and 80% methyl acetate to the NC dispersion respectively. There is still NC order visible in the sample displayed in **(c)**, but the supraparticle outline show less sharp edges. In **(d)** there is no NC order inside the agglomerates.

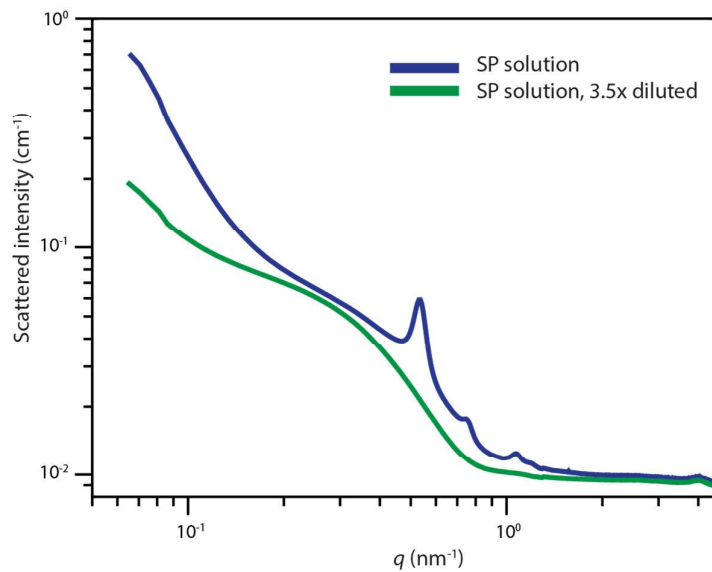


Figure S6: Transmission SAXS, showing the dissolution of the supraparticles. The solution of supraparticles in toluene (blue curve) is 3.5 times diluted with additional toluene (green curve). As can be observed, the structure factor peaks, originating from the supraparticles, disappear and only form factor scattering of the NCs in solution is observed; the supraparticles redissolve upon dilution.

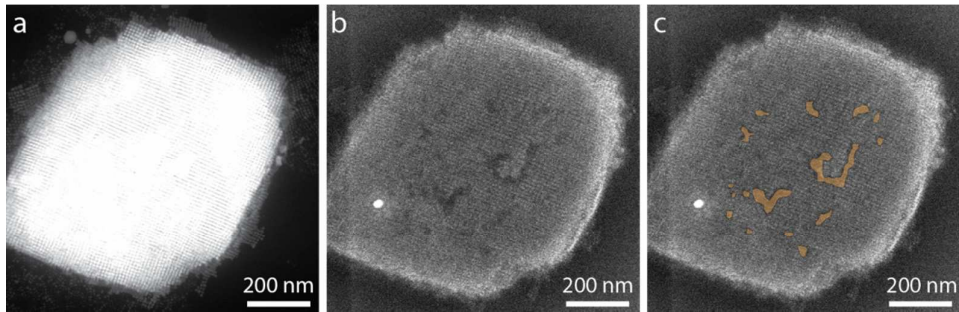


Figure S7: SE-STEM imaging of the surface of a supraparticle. (a) HAADF-STEM image of a supraparticle. (b) Corresponding SE-STEM image of the supraparticle. The missing NCs appear as darker grey area on the surface of the supraparticle. The white spot is a result of carbon build up by the electron beam. (c) For clarity, the regions with missing NCs are indicated in yellow. From all obtained SE-STEM images we estimate that the total amount of missing surface NCs equals $5.5 \pm 1.5\%$ of the total surface area of the supraparticle.

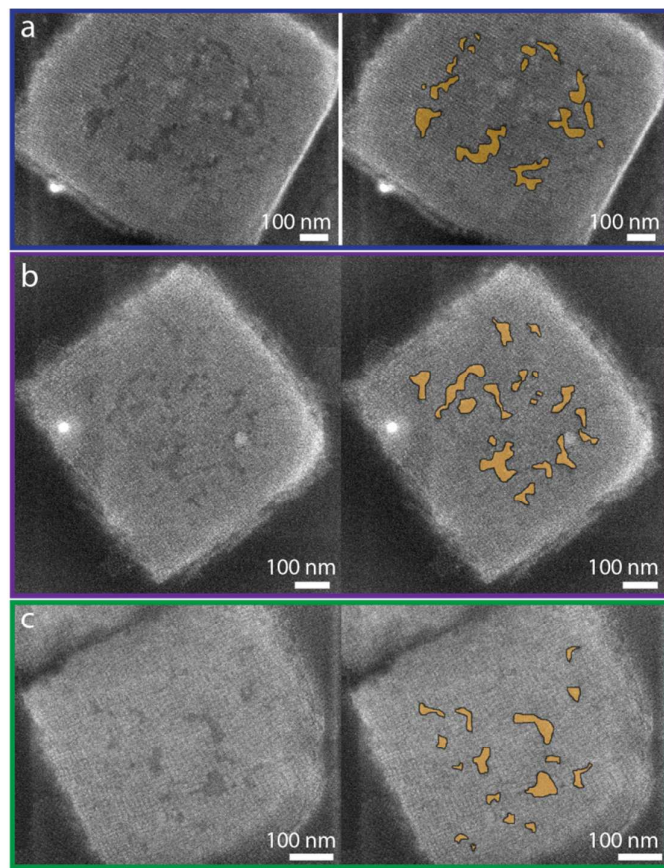


Figure S8: SE-STEM micrographs of more supraparticles, showing the presence of localized surface defects. (a-c) Images of several supraparticles, all of which contain surface defects in the form of missing (groups of) NCs. The area's containing the defects appear as slightly darker gray and are highlighted in yellow in the right column of images. We manually estimated the area of the surface defects.

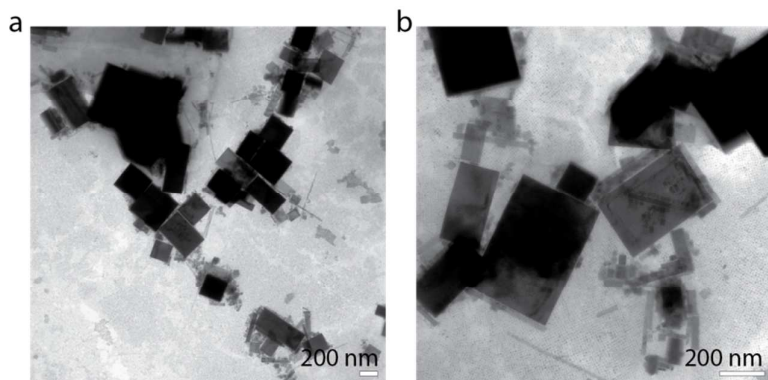


Figure S9: Formation of single crystalline particles from SPs. (a) and (b) both show bright-field TEM images of a sample which was left to incubate for two weeks in a solution with a volume fraction of 20% methyl acetate. The SPs which were observed in dispersion a week earlier seem to have transformed into single crystalline sheets of CsPbBr₃. Possibly the ligands are slowly removed from in between the NCs inside the dispersion containing the anti-solvent, allowing the NCs to fuse epitaxially. However, this remains to be verified experimentally.

High-angle annular dark-field scanning transmission electron microscopy (HAADF-STEM) tomography

The nanocube assembly was investigated using HAADF-STEM tomography. During a tomography experiment the three-dimensional object is retrieved from a set of two dimensional projection images. Only when the intensity in the measurement is a monotonic function of a property of the imaged object, they qualify as a projection². In HAADF-STEM, the image intensity scales with both the atomic number of the elements present in the sample as well as the thickness of the object, consequently fulfilling the stated requirement

Since a gap in angular range is often unavoidable due to the limited space between the pole pieces of the objective lens in the electron microscope or shadowing effects occurring at high tilt angles, this set of equations is often underdetermined, and no exact solution exists at all. Here, we will make use of the simultaneous iterative reconstruction algorithm (SIRT) in order to retrieve the 3D morphology in an iterative manner³.

A practical approach to reduce the influence of the missing wedge is to acquire a second orthogonal tilt and combine it with the former to reduce the missing wedge of information to a missing pyramid. The alignment of the tilt series was performed in the following manner. The first tilt series was aligned by using cross-correlation routines⁴. An intermediate reconstruction was then calculated and used to simulate projections along the directions where the second series was acquired. The projections of the second tilt series were then aligned through cross-correlation between the simulated and experimental projections. Using the dual tilt series as input for the SIRT algorithm we were able to enhance the quality of the tomographic reconstruction^{5,6}, as indicated by Figure S11.

We were able to visualize the nanocubes from several directions, the missing pyramid artefacts still hampered the full reconstruction of the nanocube positions. Yet, utilizing the prior information on the cubic periodicity, we can estimate the volume fraction of vacancies in the bulk of the supraparticle.

After Fourier filtering the reconstruction, the result was automatically segmented using Otsu thresholding (Figure S10 b)⁷. To determine the volume of NCs, the binarized volume was divided by the third order of the periodicity measured from a 2D intensity profile (Figure S10 b).

The volume of vacancies was found by inverting the segmented volume and removing unrealistically large connected components (Figure S10 c-d).

Combining the information from the above figure, we can conclude that:

- The assembly contains 5.529 nanocubes, accounting for a volume of 1.324.200 voxels.
- The empty space inside the superlattice equals 43894 voxels.
- The volume fraction of NC vacancies is hence roughly 3.31%.

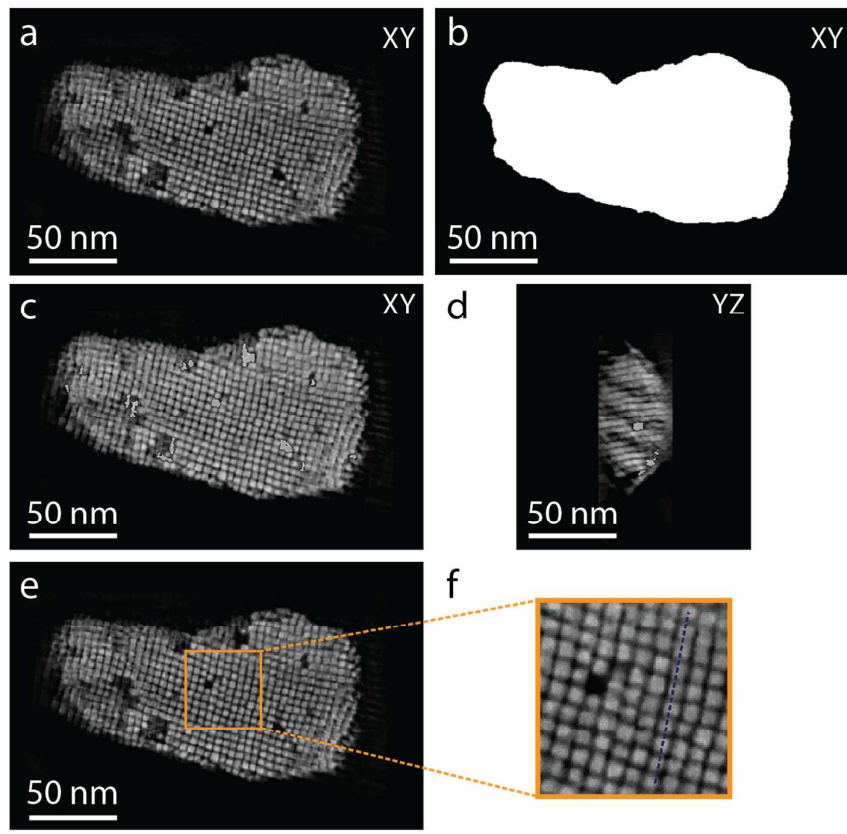


Figure S10: Determination of the volume fraction of defects in the bulk of a SP through HAADF-STEM tomography. The individual nanocubes are only well visible in the XY orthoslices (**a**) and not in the directions perpendicular to this plane. (**b**) Determination of the total volume of the SP by summing up the voxels of the segmented image. (**c-d**) Automatic segmentation of the void space inside the SP and determination of their volume. (**e**) To take into account that there exists space in between the different nanocubes, we determine the size of the cubes and the size of the gaps in between the particles (**f**).

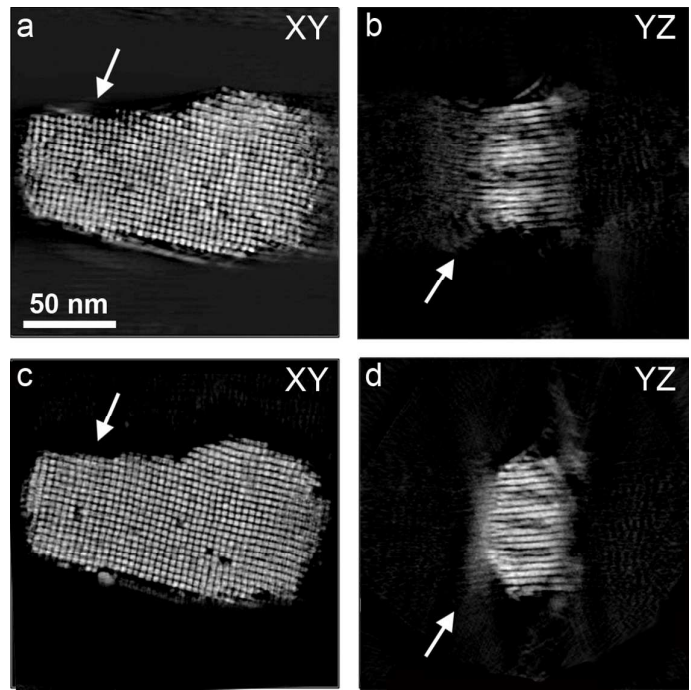


Figure S11: Quality assessment of dual tilt-axis tomography. A comparison is given between the central XY and YZ orthoslices through the SIRT reconstruction based on (**a-b**) single tilt-axis acquisition or (**c-d**) dual tilt-axis acquisition. As indicated by the white arrows, the dual tilt-axis reconstruction does not only improve the overall shape of the supraparticle in comparison to the single tilt-axis reconstruction, but it also results in a more refined reconstruction.

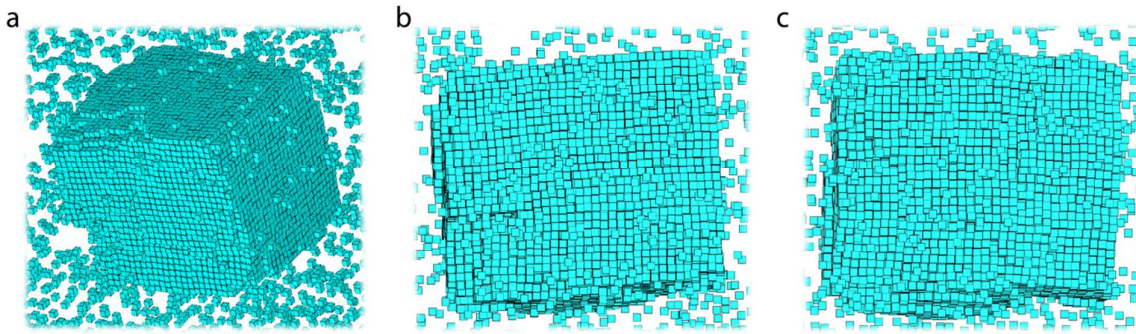


Figure S12: Monte Carlo simulations of the nucleation of the supraparticle for a system of parallel attractive cubes. (a) The nanocubes have nucleated into a ‘more or less’ cubic supraparticle. (b,c) Two different faces of the supraparticle, showing the cubic structure of the supraparticle.

We study the nucleation of a simple model system for our nanocubes. More specifically we perform Monte Carlo simulations of attractive cubes in the NVT ensemble, where N (the number of cubes), V (the volume) and T (the temperature) are fixed. The interactions between the cubes are modelled as a combination of hard-core interactions and a spherically-symmetric square well attraction. The range of the attractive square well was fixed to $\Delta = 1.14 \sigma$, with σ the edge length of the cubes, and we varied the well-depth $\beta\epsilon$ with $\beta = 1/k_bT$. Unlike in the simulations presented in Figure 5 of the main text, we fixed all nanocube orientations to be parallel for improved simulation efficiency, and did not allow any rotation of the nanocubes over the course of the simulation. Note that this is not expected to affect the nucleation product significantly.

In Figure S12, we show one typical example of a nucleated supercrystal, for an overall packing fraction of $\phi = 0.015$ and an attraction strength of $\beta\epsilon = -4.4$. From snapshots like these we always observe the nanocubes to have nucleated into a ‘more or less’ cubic supraparticle.

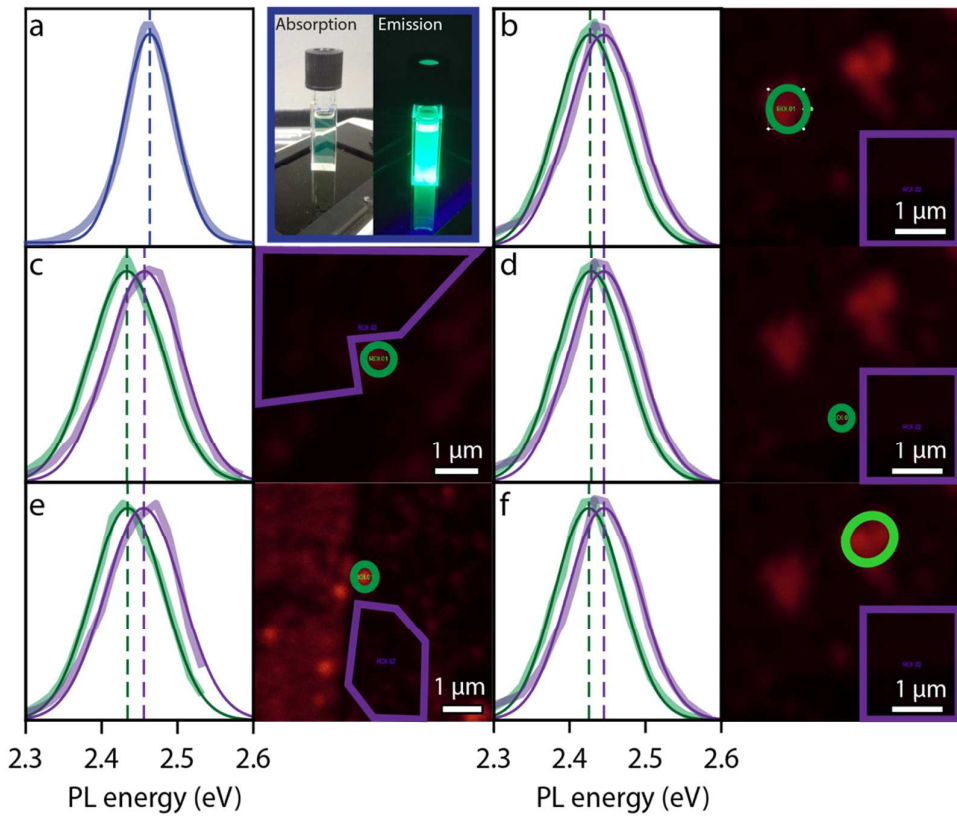


Figure S13: Additional confocal micrographs and PL spectra of single SPs. The data is shown as thick lines, whereas the Gaussian fits to the PL spectra are shown as thin solid lines. **(a)** The PL of a diluted NC dispersion. The digital photograph on the right shows the dispersion under normal daylight illumination, and illuminated by a UV lamp. **(b-f)** Various confocal micrographs and corresponding PL spectra of SPs (green) compared to the NC monolayer background (purple). In all measured spectra, we observe a consistent redshift of ~30 meV of the PL of the SPs compared to the NC monolayer background. The area in the micrograph indicates where we integrated the PL signal to obtain the displayed spectra.

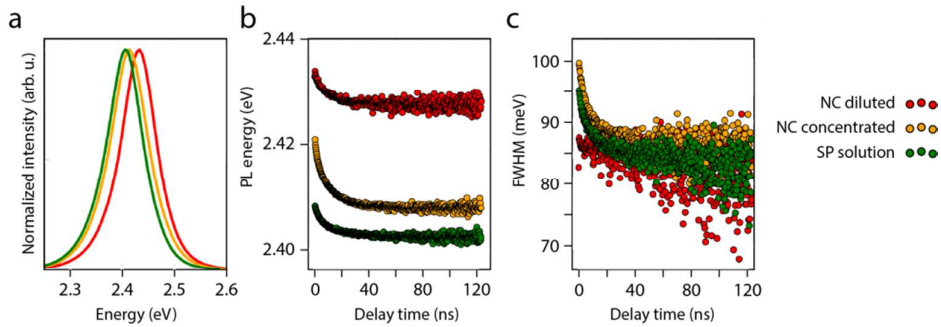


Figure S14: Time resolved emission spectroscopy (TRES) on NC and SP dispersions.

We compare solutions of NCs with two concentrations to solutions containing SPs. The concentrated NC dispersion has a concentration of $1 \mu\text{M}$ CsPbBr_3 NCs, whereas the diluted NC solution had a concentration of $10^{-3} \mu\text{M}$ CsPbBr_3 NCs. **(a)** Steady-state emission spectra of the diluted NC solution (red), concentrated NC solution (yellow) and SP solution (green). **(b)** Time evolution of the PL peak position over the first 120 ns. In all cases a redshift is observed. Research by De Weerd et al. has shown that there is the occurrence of non-radiative energy transfer between the NCs in solution through dipolar coupling or Förster Resonance Energy Transfer (FRET)⁸. We also observe a red-shift of the PL peak comparing the diluted and concentrated NC solutions. The observed redshift is increased in the SP solution. **(c)** Time evolution of the FWHM of the PL peak over the first 120 ns.

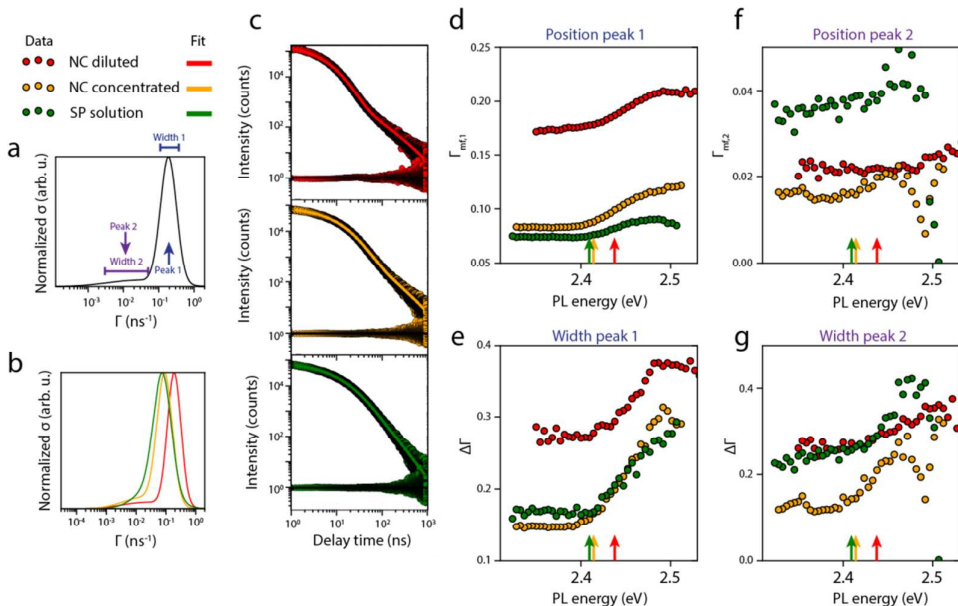
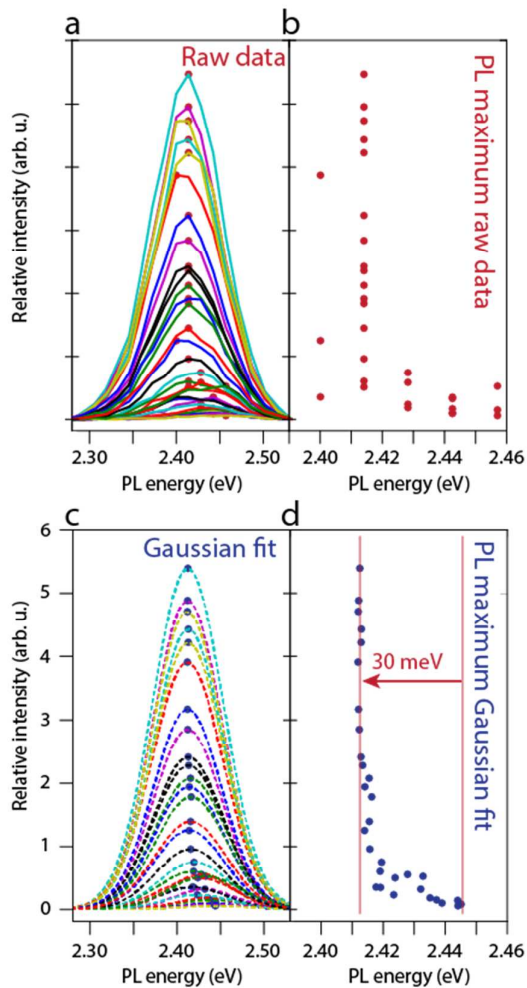


Figure S15: Time resolved emission spectroscopy (TRES) on NC and SP dispersions.

Detailed analysis of the time-resolved data. **(a)** We fit the data with the sum of two log-normal distributions⁹. The fitting procedure gives information on the distribution (or width, $\Delta\Gamma$) of two decay rates Γ . **(b)** Acquired decay rate distributions from the fits of the diluted NC dispersion (red), concentrated NC dispersion (yellow) and SP dispersion (green) as shown in **(c)**.

Analysis of the fast (**d**) and slower (**f**) decay rate components for the various PL energies and



their widths (displayed in (e) and (g)) respectively.

Figure S16: Comparison of the confocal microspectroscopy raw data and their Gaussian fits. (a) Raw PL data and the detected maximum of the peak profile. (b) Trend of intensity vs. PL energy for the raw data. (c,d) Same, but for the fitted Gaussian functions. The raw data and Gaussian fits show the same trend, i.e. the SPs emit 30 meV redshifted compared to the NC monolayer.

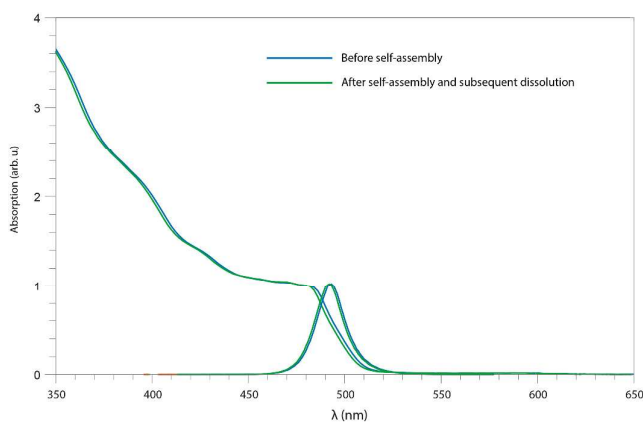


Figure S17: Comparison of the absorption and emission spectra before self-assembly of the nanocrystals and after dissolution of the supraparticles. A slight blueshift is observed, both in the emission and absorption spectrum after the self-assembly process, which might be due to some etching of the nanocrystals.

REFERENCES

- (1) De Roo, J.; Ibáñez, M.; Geiregat, P.; Nedelcu, G.; Walravens, W.; Maes, J.; Martins, J. C.; Van Driessche, I.; Kovalenko, M. V.; Hens, Z. Highly Dynamic Ligand Binding and Light Absorption Coefficient of Cesium Lead Bromide Perovskite Nanocrystals. *ACS Nano* **2016**, *10*, 2071–2081.
- (2) Hawkes, P. W. The Electron Microscope as a Structure Projector. In *Electron Tomography*; Springer US: Boston, MA, 1992; pp. 17–38.
- (3) Gilbert, P. Iterative Methods for the Three-Dimensional Reconstruction of an Object from Projections. *J. Theor. Biol.* **1972**, *36*, 105–117.
- (4) Guizar-Sicairos, M.; Thurman, S. T.; Fienup, J. R. Efficient Subpixel Image Registration Algorithms. *Opt. Lett.* **2008**, *33*, 156.
- (5) Penczek, P.; Marko, M.; Buttle, K.; Frank, J. Double-Tilt Electron Tomography. *Ultramicroscopy* **1995**, *60*, 393–410.
- (6) Mastronarde, D. N. Dual-Axis Tomography: An Approach with Alignment Methods That Preserve Resolution. *J. Struct. Biol.* **1997**, *120*, 343–352.
- (7) Otsu, N. A Threshold Selection Method from Gray-Level Histograms. *IEEE Trans. Syst. Man. Cybern.* **1979**, *9*, 62–66.
- (8) de Weerd, C.; Gomez, L.; Zhang, H.; Buma, W. J.; Nedelcu, G.; Kovalenko, M. V.; Gregorkiewicz, T. Energy Transfer between Inorganic Perovskite Nanocrystals. *J. Phys. Chem. C* **2016**, *120*, 13310–13315.
- (9) van Driel, A. F.; Nikolaev, I. S.; Vergeer, P.; Lodahl, P.; Vanmaekelbergh, D.; Vos, W. L. Statistical Analysis of Time-Resolved Emission from Ensembles of Semiconductor Quantum Dots: Interpretation of Exponential Decay Models. *Phys. Rev. B* **2007**, *75*, 35329.